Compositionally-Tailored Steel-based Materials Manufactured by Electron Beam Melting using Blended Pre-alloyed Powders

Andrey Koptyug [1], Vladimir V. Popov Jr. [2], Carlos Alberto Botero Vega [1], Emilio Jiménez-Piqué [3,4], Alexander Katz-Demyanetz [2], Lars-Erik Rännar [1], Mikael Bäckström [1]

[1]SportsTech Research Centre, Mid Sweden University, Akademigatan 1, Östersund, Sweden
E-mail: (andrey.koptyug; carlos.botero; lars-erik.rannar; mikael.backstrom)@miun.se

[2]Israel Institute of Metals, Technion R&D Foundation, Technion City, Haifa 3200003, Israel
Email: vvp@trdf.technion.ac.il

[3]Department of Materials Science and Metallurgical Engineering, Universitat Politècnica de Catalunya, Campus Diagonal Besòs-EEBE, Barcelona, 08019, Spain. E-mail: emilio.jimenez@upc.edu

[4]Barcelona Research Center in Multiscale Science and Engineering, Universitat Politècnica de Catalunya, Campus Diagonal Besòs − EEBE, Barcelona, 08019, Spain.

ABSTRACT

The paper presents the prospects of additive manufacturing (AM) in metal, using the powder bed fusion (PBF) method Electron Beam Melting (EBM) in fabrication specific steel-based alloys for different applications. The proposed approach includes manufacturing of metals from blended pre-alloyed powders for achieving *in situ* alloying together with the material microstructure tailoring by electron beam energy deposition rate control. EBM tests were conducted with the blends of 316L stainless steel and Colferoloys 103 and 139, corrosion and abrasion-resistant iron based materials commonly used for plasma spray coating. Thorough microstructure analysis of the manufactured sample was carried out using electron microscopy, and measurements of microhardness and elastic modulus was carried out using nanoindentation. It is concluded that implementation of blended powder pathway in PBF AM allows to widen the scope of available materials through diminishing the dependence on the availability of pre-alloyed powders. Together with beam energy steering this pathway also allows for an effective sample microstructure control at different dimensional scales, resulting in components with unique properties. Therefore, the implementation of 'blended powder pathway' in PBF AM provides a possibility of manufacturing components with the composite-like and homogeneous zones allowing for the microstructure control and effectively adding a "4th dimension" to "3D printing".

Keywords:
Additive manufacturing; Electron Beam Melting, EBM; *in situ* alloying; graded material; blended powder

GRAPHICAL ABSTRACT
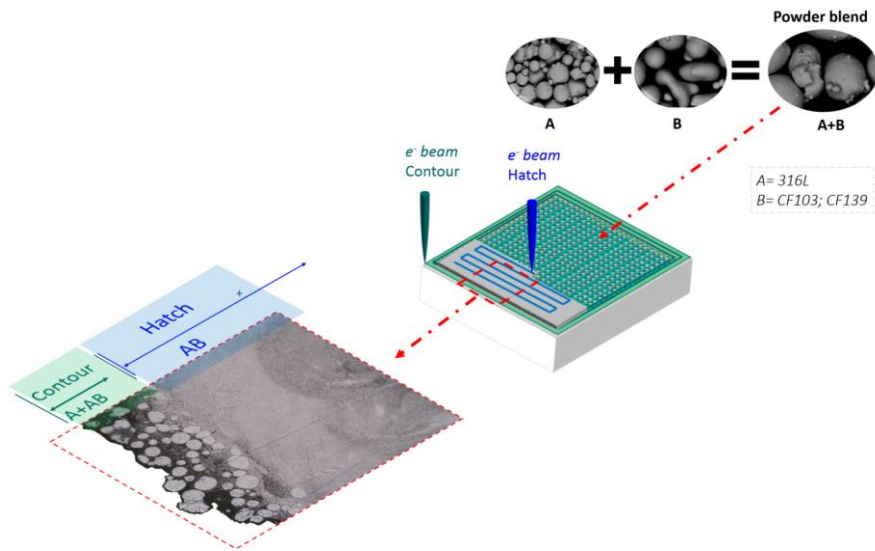
1. Introduction

Additive manufacturing (AM), often also called 3D-printing, is a family of an innovative technologies using layer-by-layer material deposition. Started as a prototyping technology using polymers AM today utilizes large variety of materials including elemental metals and alloys [1, 2]. Most commonly cited advantage of AM is an unprecedented freedom of component shapes achievable with AM methods. This is entirely true for the powder bed fusion AM technologies (PBF) including Electron Beam Melting (EBM), which use a metallic powder as precursor material [3-5].

Traditionally PBF additive manufacturing employ fully pre-alloyed powders in order to obtain required chemical composition, desired microstructure and uniform properties of the products. Today existence of appropriate and stable production routes of pre-alloyed powders is presumed an obvious way for achieving consistency and required quality in production of components using PBF AM technologies. So the majority of the AM production including critical parts for aerospace and defense industries made of Ti-based alloys and Ni-based superalloys [6], Ti-based alloys for implants used in biomedicine [7, 8], rare-earth and non-rear-earth based permanent magnets [9-12] is performed using pre-alloyed powers with homogeneous elemental composition, microstructure and grain size distributions. The same time automotive, aerospace and biomedical sectors being so far the largest beneficiaries of AM technologies are continuously expressing the need for expanding variety of materials available for AM. In addition, the manufacturing of pre-alloyed powders for some promising materials is expensive, is not developed at all or is not available at needed industrial scale. In some cases, like with the high entropy alloys, pre-alloyed powders are hardly possible [13]. Thus, a search for modalities bypassing the restrictions imposed by the lack of pre-alloyed powders for AM is becoming one of the promising routes for reaching new materials with unique properties.

One of such possibilities is in using blends of elemental or easily available pre-alloyed powders and performing *in situ* alloying. Additional interest towards the powder blending in PBF AM is related to the possibilities of manufacturing components with composite and composite- like structure [4, 14], and steering the material microstructure in three dimensions inside the component during its manufacturing [15-19], which can be referred to as "4D-printing".

In the present paper, we report on the investigation of both *in situ* alloying of the two iron-based powders with EBM, and on the adjustment of material structure producing by choice the composite-like and alloyed material from the same precursor powder blend by adjusting the electron beam energy deposition rate. For this study we have chosen stainless steel 316L (SS316L), and Colferoloy 103 and Colferoloy 139 (hard, abrasive and corrosion resistant alloys commonly used for plasma spray coating). In general, steels and iron-based alloys in general are so far the most commonly used industrial materials. Moreover, a possibility of manufacturing components with abrasive and corrosive resistant periphery and ductile core in one manufacturing process seemed quite attractive. This approach was also regarded as a step to achieving composition and functionally graded materials with electron beam melting technology, and to manipulating the material microstructure within a component during additive manufacturing process.

2. State of the art

Present chapter describes current state of the art in PBF manufacturing of SS316L; melting-cooling conditions specific to PBF methods and the consequences such conditions can have to the material microstructure and properties; *in situ* alloying; powder blend application and manufacturing of Structurally / Functionally Graded Materials using PBF AM.

Additive manufacturing of steels, in particular of stainless steel 316L, is not a novelty as such. There is a significant number of publications describing different AM approaches to its

manufacturing [2, 20-24], specifics of laser- and electron-beam based PBF manufacturing processes used for SS316L, characteristic microstructure of additively-manufactured SS316L and its mechanical properties [21, 25-35]. In many cases, authors are comparing the properties of AM-manufactured SS316L samples with the ones reported for the same material manufactured by more traditional methods.

A number of researchers reported on SS316L manufacturing by laser-based AM methods, in particular by laser-based PBF (L-PBF) [2, 21, 22, 24, 28, 31, 34, 36]. Characteristic microstructure of the achieved materials is predominantly hierarchical and austenitic with 10 to 25 μm sized grains containing fine 1 μm- sized subgrains with a cellular microstructure [2, 21]. Partial phase austenite to ferrite transformation at high temperatures characteristic to L-PBF melt pool cooling dynamics combined with the growth of subgrains inside the micron-sized grains and nucleation of the sigma phase can promote the tensile strength of SS316L to 300 MPa at 1100° C compared with approximately 40 MPa of conventionally manufactured 316L. The observed grain microstructure in L-PBF manufactured material may and superior resulting material properties can potentially change the application criteria for SS316L as a construction material and expand its application fields. The fabrication of SS316L with different laser beam spot size ("focused" and "defocused" modes) in L-PBF resulted in only few micro-cracks occurring in approximately 95.54% dense samples demonstrating excellent mechanical properties [2]. Samples manufactured with both beam strategies exhibit the typical ductile fracture with many dimples [2]. The same time, some researchers report that ductility of the laser-based additively manufactured SS316L is some lower, and hardness- higher than that of the samples manufactured using more traditional methods [34]. That could be explained by the reported dislocations accumulation on sub-grain boundaries. This conclusion is supported by the decrease of the microhardness values recorded for as manufactured

5

components and after they are subjected to annealing at 800˚C for 6 min under argon atmosphere from 3.2 ± 0.1 to 2.2 ± 0.2 GPa correspondingly.

Research was also conducted for evaluating the effect of the process parameters in L-PBF. Kurzynowski et al. (2018) have studied the influence of applied laser power and beam scanning strategies (alternating traces without and with re-melting after each layer) microstructure of resulting SS316L material [31]. No significant changes of tensile strength and elongation were found for the samples manufactured with different parameter settings chosen. Material microstructure of as-manufactured components was similar to the one reported by other authors and consisted of columnar grains of austenite with intercellular segregation of Si, Cr and Mo, but additional formation of non-equilibrium eutectic ferrite have been revealed. Authors have also reported that for as-manufactured components and even after the post-processing residual stress inside the material was still higher than that common for SS316L after hot rolling. Such situation with reasonably high internal stress in as manufactured components is quite common for the L-PBF AM methods. With EBM residual stress in as-manufactured components is much less pronounced, as the components are kept at elevated temperatures through the entire manufacturing process providing continuous annealing [4, 5].

Manufacturing of SS316L components by EBM was also reported [27, 29, 32, 33]. In this case research was aiming to utilize unique properties of SS316L including its excellent stability when subjected to extreme temperature cycling for nuclear applications. Comparison of the microstructure for the EBM-manufactured SS316L shows similarities with the one reported for the one manufactured with laser-based PBF AM methods, but differences are also present. Formation of hierarchical structures in EBM-made SS316L sample microstructure is observed [27, 29, 32], similarly to the one detected for the samples manufactured by laser-based methods. The same time, clearly pronounced hierarchical microstructure is characteristic mainly for the last deposited layers of the samples, and it was gradually changing towards the

6

first layers, with the hierarchical microstructure becoming less and less pronounced [27, 32]. This microstructure heterogeneity is attributed to the different thermal history of the corresponding material layers in the sample kept at the elevated temperature throughout all EBM manufacturing process. First deposited layers are subjected to the effective annealing for significantly longer time as compared to the last deposited layers. And hierarchical structures with the columnar grains, characteristic to the consecutive re-melting of few material layers and fast solidification in presence of strong temperature gradients directed along the sample from its top towards bottom are gradually 'erased' by effective annealing. Simultaneously with the disappearance of the hierarchical structures, the grain boundaries become more and more pronounced towards the first deposited material layers. Despite the local enrichment of molybdenum in cell and grain boundaries, austenite was observed to be a dominating phase throughout the entire sample, with less than 0.5% other phases. No difference in microhardness has been detected at various sample locations. The strength and ductility of EBM as-manufactured SS316L was found to decrease at high temperatures, but increased toughness at 250ºC was also recorded [29]. This was attributed to the pinning effects of the sub-grains, which strengthen EBM manufactured SS316L while keeping good ductility and toughness.

The impact of the microstructure homogeneity was specifically addressed in the research by Günther et al. [30], stressing the value of isotropic microstructure and high defects tolerance in newly designed materials for AM. It was concluded that alloys solidifying into cubic crystal structures are commonly affected by strong anisotropy due to the formation of columnar grains of preferred orientation. Moreover, processing itself often induces defects and porosity detrimentally influencing static and cyclic mechanical properties. Nevertheless, authors reported that the EBM processed Cr, Mn and Ni containing metastable austenitic steel was extremely damage tolerant under monotonic loading and characterized by low sensitivity to

7

process-induced defects due to the high local strain-hardening and delayed necking triggered by the TRIP effect [30].

A fabrication of austenitic SS316L specimens with 76% increase in the yield strength and a corresponding increase of 29% in the ultimate tensile strength comparable to the commercial forged SS316L stainless steel by means of EBM was reported by Segura et al. [33]. Thus, PBF-AM may offer a new way to produce steel-based components with pre-designed microstructure providing extraordinary properties. Nevertheless, the challenges of obtaining desirable microstructure and density by AM (in particular for large components) still remains as this study indicated a presence of numerous pores and their undesirable distribution in sub-surface regions in the AM steel [28].

Development of new materials and modalities can successfully utilize unique conditions characteristic to the PBF AM methods [5, 14, 28]. Most critical for these is uniquely high beam energy density reaching 10^{10-12} W/cm^2 for laser-based and even higher for electron beam based PBF methods. Local material heating rates can reach 10^{6-7} K/s with just some lower cooling rates up to 10^{5-6} K/s, with the melt pool temperatures few thousands K above melting points of the majority of metals and alloys. Time window from melting to solidification of the material in each particular spatial point of the layer is often down to 10^{-3} s. So PBF AM methods provide unique non-equilibrium metallurgical conditions, allowing speaking of entirely new, non-stationary metallurgy [4, 14] not only preserving some metastable states in the sample microstructure, but also producing non-equilibrium materials like high entropy alloys [13] and amorphous or bulk metallic glass materials [25, 37-39].

Unique conditions of PBF AM methods also appear to be favorable for the manufacturing of matrix and composite materials. Few studies were reported on the successful manufacturing of metal-ceramic composites: SS316L + tungsten carbide [5] by EBM, tungsten carbide + cobalt

8

by L-PBF [40], Ti6-Al4-V and tungsten carbide by cladding [41], and more complex ones - WC/NiBSi by EBM [42], and (TiB + TiC)/Ti by electron beam surface melting [43].

So far, most of the research activities in this direction were devoted to the *in situ* alloying. It was performed by PBF AM using blended powders from elemental materials like Mn+Al by EBM [11], Al+Cr+Mo+Nb+Ta by EBM [13], SS316L+W by EBM [14], Ti+Al+V by laser-based AM [44-45], Fe+Cr+Ni by direct energy deposition (DED) [46], Al+Si by L-PBF [47], Ti+Nb by L-PBF [48], Ti+Ni by DED, L-PBF and EBM [36], Ti6Al4V+Ti45Al7Nb by EBM [49], SS316L with a number of different iron based materials by EBM [14]. Interest for utilizing blended materials is continuously growing, forcing the development of special hardware [50] or modifications of existing AM machines [14]. Using such novelties manufacturing of graded materials (gradually changing composition, structure and functionality) becomes possible [5, 14, 44, 46, 50-52].

Along with this, new pathway for additive manufacturing of composite and matrix materials using "composite powders" is starting to rapidly develop. For example it was reported on the manufacturing of nanostructured composite WC-Ni by Lima et al. [53], of nanoreinforced Ti powders by Fernández-Roiz et al. [54] and reinforced Al powders by Martin et al. [55].

Present research was inspired by the desire of using relatively inexpensive widely used iron based materials for making something like a Damascus steel [56] combining ductility of the component cores with hardness of their periphery. Basing on previous feasibility studies, availability of the modified hardware [5] and previous experience with material development for EBM in general and iron-based materials in particular [4, 6, 10, 13, 14, 27, 29, 32, 37] EBM experiments with powder blends of SS316L steel and two iron based materials commonly used for plasma spray coating were performed targeting *in situ* alloying and matrix material.

3. Materials and methods

Experiments were carried out in the ARCAM A2 machine by ARCAM EBM [57] with the modified powder delivery system tailored for smaller powder batches [5]. Used powders were acquired from two different sources: stainless steel 316L powders from Carpenter Powder Products AB [58]; Colferoloy 103 (CF103) and Colferoloy 139 (CF139) from Wall Colmonoy Corporation [59]. Colferoloy is the family of highly alloyed, iron-based hard, corrosion and abrasion resistant alloys designed for plasma spray coating [60-62]. Measured compositions of the used powders are presented in Table 1. Elemental compositions of used powders coincide with manufacturer specifications listed in corresponding datasheets. Powder grain sizes distributions of both powders are close the one suggested by ARCAM EBM [57].
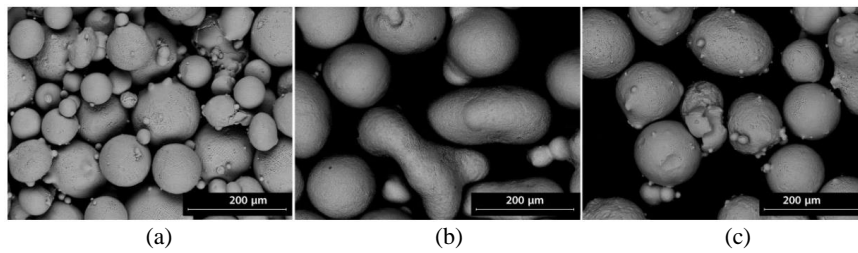

| | (a) | (b) | (c) |

Figure 1. SEM images of the used powders: (a) SS316L, (b) ~~Colferoloy~~ CF139, (c) ~~Colferoloy~~ CF103. CamScan MV2300 SEM, backscatter detector, magnification x500.

Table 1. Measured elemental compositions of the used powders

	C	Mn	Si	Cr	Ni	Mo	P	S	N	B	Non-Fe, %	Fe, %
SS316L	0.03	1.5	0.7	17	13.5	2.5	0.045	0.03	0.1	0	35.405	64.595
CF103	0.6	-	-	32	8	-	-	-	-	4.6	40	60
CF139	0.75	-	-	20	-	-	-	-	-	5	25	75

Figure 1 presents typical SEM images of the used powders (SEM CamScan MV2300 with BS102 BSE detector by K.E. Development Ltd., Cambridge, UK). All powders have close to spherical grains with small amount of satellites, but both Colferoloys have narrower grain size distributions, and ~~Colferoloy~~ CF139 has more elongated grains. Hall flowmeter powder flow

test values were within the limits recommended by ARCAM EBM. All powder blends were prepared manually by shaking and rolling for 45 minutes in a glass container (this can be advised for fast screening experiments only). One can refer to the review by Vock et al. [63] for a comprehensive discussion on powder-related issues in powder bed AM.

Three specific compositions were investigated: pure SS316L and two powder blends, (SS316L+CF103) and (SS316L+CF139). For these experiments, volumetric fraction ratios of the individual powders were used: 4/1 for SS316L/CF103; 4/1 and 4/3 for SS316L/CF139.

Detailed sample characterization was carried out for 4/1 vol. ratios of the powder blends. Prismatic samples with the base 10x10 mm^2 and height 15 mm were manufactured with the melting beam parameter settings adjusted from the set developed for the EBM manufacturing of pure SS316L and layer thickness set to 200 μm. As common for the ARCAM EBM, two melting strategies are used in each sample, 'contours' and 'hatching' [19, 64].

First, the beam melts a periphery of what would be a solid sample by running round the circumference, and then by the raster motion melts the inner part. In production, these strategies allow for better spatial resolution and improved component surface roughness. In current experiments, it was used as an easy mean to apply different melting strategies within a single sample. Within each layer two continuous slightly offset contour passes are performed for each sample with beam line energy LE~ 1.2 J/mm (estimated averaged beam area energy in the contour parts of the samples is AE~ 1.7 J/mm^2). Raster 'snake' scan in the 'hatch' (core) part of the samples is carried out with area energy AE~ 5.2 J/mm^2. For the LE and AE calculations following common expressions were used:

$$LE[J/mm] = \left. Beam\ power[W] \middle/ Scan\ speed\ [\tfrac{mm}{s}] \right. \tag{1}$$

$$AE[J/mm^2] = \left. Beam\ power[W] \middle/ \left(Scan\ speed\ \left[\tfrac{mm}{s}\right] * Line\ offset[mm]\right) \right. \tag{2}$$

11

The microstructure investigation was performed on the samples carefully removed from the start plate using High-Resolution Scanning Electron microscopy (HR-SEM), and High-Resolution Transmission Electron microscopy (HR-TEM). The microstructure and element concentration of manufactured samples were studied using a scanning electron microscope Zeiss Ultra-Plus FEG-SEM equipped with microanalyzer. The SEM microstructure investigation has been performed on the polished (not etched) samples cut perpendicular to the build direction (z-axis), e.g. following the layer plane.

For the TEM investigation, disk-shape samples with the average diameter of 3 mm were prepared from the printed cubes by subsequent ion polishing and plasma cleaning. The high-resolution transmission electron microscopy images, high-angle annular dark-field scanning transmission electron microscopy (HAADF-STEM) images and electron dispersive spectroscopy (EDS) maps were acquired using a monochromated and double corrected Titan Themis G2 60-300 (FEI / Thermo Fisher) unit operated at 200KeV and equipped with a DualX detector (Bruker). The quantitative analysis of the EDS maps was done using the Velox software (FEI / Thermo Fisher).

Samples for the nanoindentation tests were encapsulated in acrylic resin, upper layers of the sample were ground down to remove 0.5 mm from the top of the sample parallel to the manufacturing layers. Samples were then polished with consecutively finer grit down to $3\mu m$, with a final fine polishing step using colloidal silica slurry for 15 minutes. An EBM-manufactured SS316L sample was tested as a reference together with the samples manufactured from the blended powders.

Nanoindentation tests were ~~approached~~ applied accounting for the length scale of microstructural features (hierarchical-like microstructure) typical for a cast SS316L, and known for the EBM manufactured SS316L sample. Typical SS316L microstructure consists of the grains with the sizes up to 50-200 µm and sub grains down to 1-5 µm configuring a cellular-

12

like substructure [27-29, 30, 32]. The effect of different length scales on the mechanical properties is investigated by using two approaches with regard to the maximum penetration depth of the tests (h_{max}). Nanoindentations at h_{max}= 2000nm were conducted aiming to investigate the overall mechanical behavior of materials (indentation zone affects several subgrains). Tests with h_{max}=200 nm were conducted to investigate the individual behavior of subgrains, as well as the contribution of the subgrain boundaries and precipitated phases on the overall mechanical properties. Matrices of 4 x 4 indentations were used for the core of the samples (away from the sample edges). Separation between indentations was 25 times h_{max}. Tests were carried out in a MTS Nanoindenter XP at a constant strain rate of 0.05 s^{-1} using a Berkovich indenter with its area function calibrated using a fused silica standard sample. The continuous stiffness measurement (CSM) modulus was activated so that the load (P), penetration (h), and the contact stiffness (S) were continuously recorded. Hardness (H) and elastic modulus (E) were evaluated as a function of the penetration depth based on the model proposed by Oliver and Pharr [65] and Pharr et al. [66].

For characterization of residual imprints after nanoindentation tests at the surface level, and to account for the microstructural features of manufactured materials, samples were etched using Kroll reagent for 25 minutes, and subsequently imaged both by Optical Microscopy (OM) and SEM. In the specific case of SS316L+CF103 sample, and in order to investigate the indentation scenario at the subsurface level, a cross-section of a single indentation trace was prepared using the Focused Ion Beam (Zeiss Neon 40) coupled to a Field Emission Scanning Electron (FE-SEM) microscope (Neon 40, Carl Zeiss, Oberkochen, Germany). An imprint performed with $h_{max} = 2000$ nm was first selected and imaged, and then cross- section was prepared and imaged again. In the indentation area, FIB trenches were produced using a Ga+ ion beam directed normally to the sample surface with decreasing currents. Final polishing step with a beam of 50 pA at 30 kV was used to reveal the residual imprint under the indentation and its interaction

with the microstructural features of the material. Finally, a SEM images were acquired. The dimensions of the trenched cross-section are 5 x 15 µm, which was enough to cover several grains.

Corrosion tests aimed to investigate the possible decrease of corrosion resistance in the CF103/CF139-based printed composites, as the amount of carbon in Colferoloys is more than 0.6. Determination of corrosion susceptibility for EBM- manufactured SS316L-based samples with additives was performed by electrochemical cyclic polarization technique.

4. Results and discussion

4.1 Sample Microstructure

Two different types of the microstructure were observed in the samples: a composite-like one at the contours of samples, where two distinct phases can be discerned, and a metastable fine microstructure at the core, resembling the typical sub-grain cellular structure found on additively manufactured SS316L with well-defined precipitated phase on the cell boundaries (see Figure 2). In the backscatter image presented in Figure 2 the composite-like microstructure found at the contours of the sample can be clearly observed: brighter, rounded areas are SS316L-enriched (almost 100% SS316L), surrounded darker phase is Colferoloy-rich (almost 100% Colferoloy). SS316L inclusions show the presence of boron and enrichment in chromium coming from Colferoloy across the whole volume.

By changing the melting beam energy depositions strategy one can vary not only the microstructure of the additively manufactured components at the grain- and subgrain level [15-19], but also turn from the composite-like to homogeneous sections within each component [14].
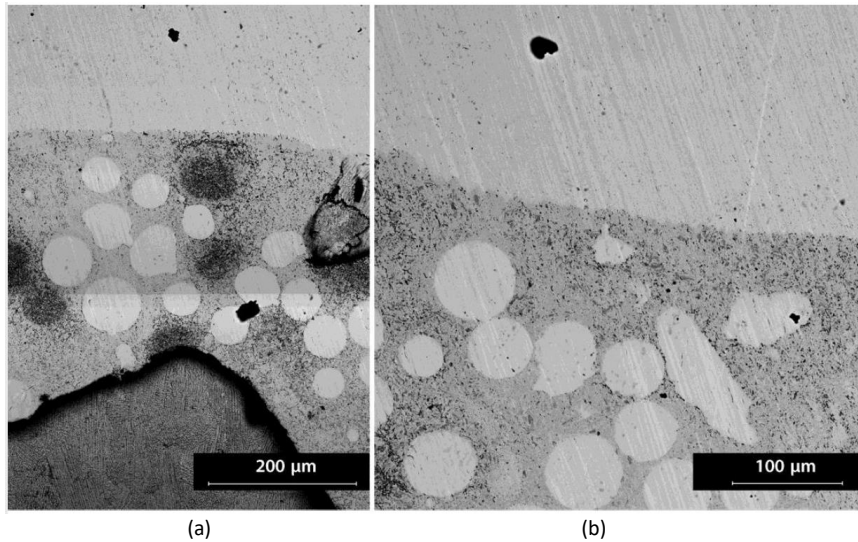
Figure 2. Typical SEM image of the sample edge performed using 'contour' (bottom of the images) and 'hatch' (top of the images) melting settings. Zone separation is clearly visible near the upper third of the images. Samples are made from the powder blends of SS316L and ~~Colferoloy~~ CF139 (a) and ~~Colferoloy~~ CF103 (b). CamScan MV2300 SEM, backscatter detector. Samples are cut, polished and etched in Kroll reagent

Composite-like zones at the periphery of the samples result from the melting with faster beam having smaller line and volume energy, as compared to the melting in the core sample parts. It is feasible, that with deeper and wider melt- pool at the 'hatch' (core) area of the samples, and with consecutive re-melting material spends longer time in molten state resulting in almost complete homogenization. One can speculate that what we see in two-phase periphery ('contour') is a result of molten phase solidification, rather than a presence of solid SS316L grains in solidifying molten Colferoloy. If so, the result may be due to the difference in the surface tension of the two materials and specifics of the diffusion of SS316L into Colferoloy at the melt pool temperatures.
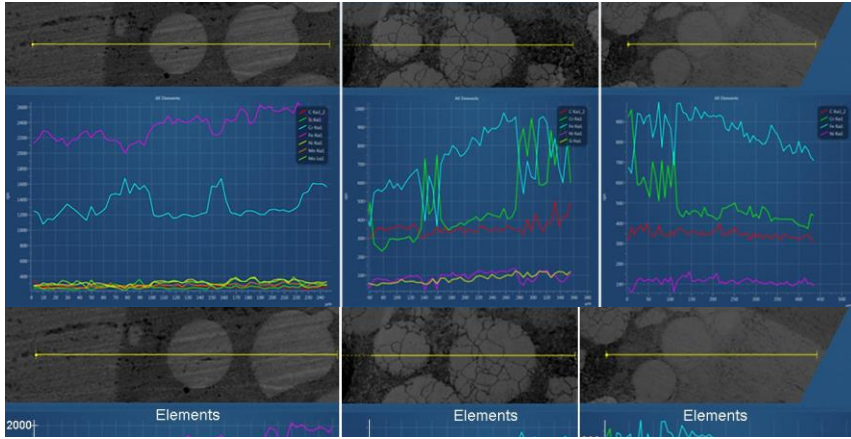
Formatted: Highlight

Figure 3 provides typical EDS mapping of the SS316L +CF Colferoloy 139 samples. Tables 2 and 3 provide the composition data measured by EDS in representative elements of all three zones for SS316L + CFColferoloy 139 and Colferoloy CF103 correspondingly, in comparison to the specifications of the used powders. Data analysis indicates, that in the 'contour' zone composition of round areas corresponds to predominantly SS316L, while the 'matrix' surrounding them- to Colferoloys. Most clearly, this is illustrated by the content of Cr, Mo, Mn, B and Ni in thecae of SS316L+CF139 blend. In the 'contour' composite-like area, there is certain deflection in the elemental composition of the round and 'matrix' zones from the composition of corresponding powders. In addition, there is some difference in elemental compositions between similar zones in different parts of the composite-like 'contour' area. This is an indication that certain intermixing of the materials took place. Material composition in the core area is rather similar for all parts of the 'hatch' area.

Table 2. Elemental compositions for three distinct zones in the 'contour' and 'hatch' zones for SS316L+ ~~Colferoloy~~CF139 samples (measured values are listed together with standard deviation).

Elements, Wt%	C	Mn	Si	Cr	Ni	Mo	B	S	Fe
SS316L+CF139, composite, round	6.63 ±0.25	1.45 ±0.15	0.55 ±0.05	17.54 ±0.19	11.38 ±0.27	--	--	0.75 ±0.06	61.70 ±0.33
SS316L+CF139, composite, matrix	9.08 ±0.41	0.94 ±0.14	0.81 ±0.05	20.85 ±0.62	9.10 ±0.34	1.59 ±0.15	7.15 ±2.59		50.47 ±1.44
SS316L+CF139, core	11.06 ±0.46	1.10 ±0.13	0.50 ±0.04	16.17 ±0.48	9.47 ±0.35	2.04 ±0.15	8.87 ±2.54	--	50.78 ±1.45
SS316L, nominal, ASTM A240	0.03 max	2.0 max	0.75 max	16 to 18	10 to 14	2 to 3	--	0.03 max	to 100
CF139, Supplier specifications specs	0.75	--	--	20	--	--	5	--	74.25

Table 3. Elemental compositions for three distinct zones in the 'contour' and 'hatch' zones for SS316L+ ~~Colferoloy~~CF103 samples (measured values are listed together with standard deviation).

| Elements, Wt%	C	O	Mn	Si	Cr	Ni	Mo	B	S	Fe
316L+CF103, composite, round	--	--	1.32 ±0.14	0.34 ±0.04	11.54 ±0.76	8.09 ±0.56	1.31 ±0.24	36.10 ±4.17	0.00 ±0.08	41.29 ±2.70
SS316L+CF103, composite, matrix	--	2.91 ±0.18	0.65 ±0.14	0.69 ±0.05	26.13 ±1.00	5.71 ±0.29	1.69 ±0.14	24.13 ±2.84		38.11 ±1.45
SS316L+CF103, core	--	--	0.89 ±0.13	0.45 ±0.05	14.77 ±0.98	8.39 ±0.59	1.12 ±0.26	29.14 ±4.63	0.10 ±0.08	45.14 ±2.96
CF103, supply, specs	0.6	--	--	--	33.75	8.18	--	4.06	--	--
SS316L, nominal, ASTM A240	0.03 max	--	2.0 max	0.75 max	16 to 18	10 to 14	2 to 3	--	0.03 max	balance
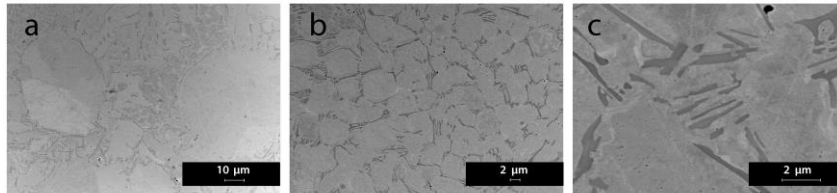
Figure 4. SEM images of composite like material EBM-manufactured from SS316L and CF103 powder blend: a, b –homogenous microstructure with the main light austenite-based phase and dark grain boundaries; c –higher resolution image of the two main phases.

Typical microstructure of the core zone in the EBM as-built SS316+CF103 (4/1vol.) specimens is shown in Figure 4, and EBM as-built SS316L+CF139 (4/1vol.) specimens - in Figure 5.
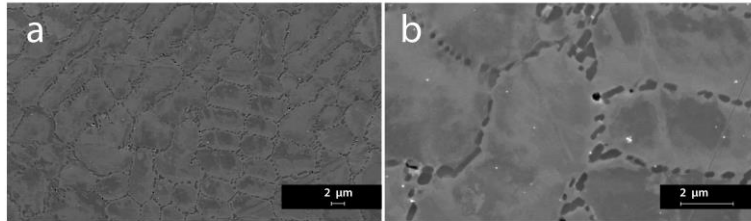
Figure 5. ~~SEM~~ (back-scattered) images of composite like material EBM-manufactured from SS316L and CF139 4/1 vol. powder blend: a – the ~~homogenous mm~~microstructure ~~of~~ ~~with the mm~~ain ~~light~~ austenite-based phase (looks as bright) with homogeneously dispersed at grain boundaries Chrome/Boron rich phase (looks as dark)~~, with the dark phased grain boundaries~~; b – higher resolution image of the two main phases.

According EPMA measurement results, samples manufactured from blended powders exhibit a fine microstructure (Figures 4, 5), similar to the cellular one exhibited by EBM of pure SS316L, consisting of austenite-based (~~light~~bright) SS316L-dominated grains and a precipitated grain boundary phase (dark) enriched by the elements coming from Colferoloys. Morphology of the boundary phase is mainly lamellar. It should be noted that, in general, the austenite-based grains are equiaxial with relatively similar grain size of 3 to 10 μm. But some sample zones contain extremely large (up to 60 μm) austenite-based grains as illustrated for SS316+CF103 in Figure 4a. The most probable reasons for the existence of such large grains are inhomogeneous powders blending and local differences in the grain sizes, and non-uniform cooling rate in and around the melt pool. With the powders having relatively wide grain distribution, completely homogeneous mixing is hard to achieve, as smaller grains tend to form clusters and in some cases are "coating" larger grains. EBM-manufactured samples of SS316L+CF139 with 4/3 volume ratio of the initial powders in general exhibit very similar microstructure to the one obtained for the 4/1volume ratio samples.

Microstructure of the zones in the composite-like 'contour' area is very similar to the one for the core in used powders. Interestingly, the 'matrix' at the sample periphery is represented by corrosion- and abrasion- resistive hard Colferoloys, with ductile SS316L phase inclusions. The

same time, 'core' material also has composite-like microstructure, with the larger grains surrounded by rather wide grain boundary zones. Thus, additive manufacturing using blends of hard and ductile materials together with beam energy deposition steering has a serious potential for industrial manufacturing of the components having composite-like and homogeneous sections in a single process. For example, one can manufacture components with reasonably ductile core and composite-like corrosion- and abrasion-resistive surface areas and hard reinforcing elements inside.

4.2 TEM characterization of SS316L+CF103 samples

Typical TEM bright field (BF) image microstructure of the near grain boundary zone (triple junction) is shown in Figure 6. According to TEM EPMA data analysis the main (light) areas correspond to austenitic-base phase inherited from SS316L, while the dark grain boundary areas corresponds to Colferoloy-dominated phase. Element content mapping confirms that Fe and Ni are found mainly in the austenite phase (SS316L has high Ni content, see Table 1), while grain boundary phase is enriched in Cr and B (characteristic to CF103). Mn, O and C are homogeneously distributed in both the grains and the grain boundary phase. Some excess amount of Mo is observed at the grain boundaries. Presence of the oxygen in the manufactured samples can be explained by the powder surface oxidation in storage and handling.
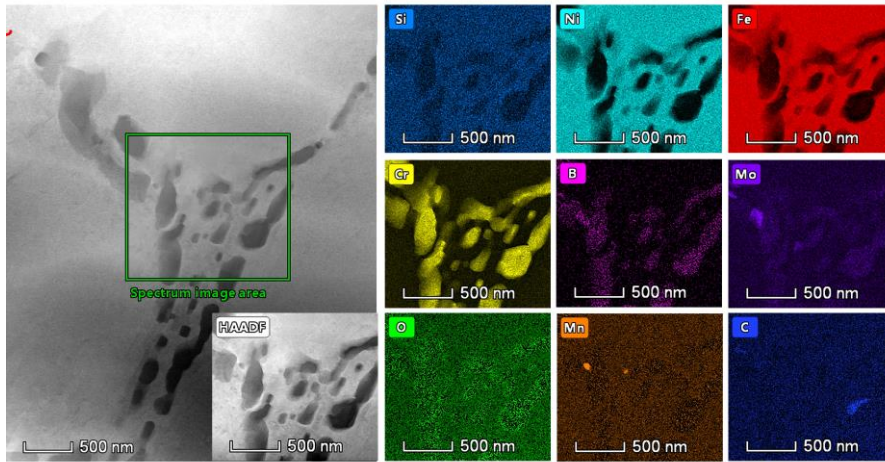
Figure 6.TEM-image and composition maps for the composite like material EBM-manufactured from SS316L and CF103 4/1 vol. powder blend

Following conclusions about the elements transfer occurring during manufacturing process can be formulated:

- Iron and nickel diffuse out of Colferoloy- dominated grain boundary phase into the austenitic matrix.

- Molybdenum and especially chromium diffuse out of austenitic SS316L-dominated phase into Colferoloy- dominated grain boundary phase

- Boron mainly carried from Colferoloy had not diffused to B-poor volumes of austenite, and grain boundary phase consists mainly of Cr-B rich phase.

4.3 Nanoindentation tests

Optical image of typical residual imprints of the 4x4 nanoindentation matrices with h_{max}= 2000 nm and 200 nm, conducted on the SS316L+CF103 sample core area is presented in Figure 7. The matrix of the larger indentations correspond to the tests with h_{max}= 2000 nm, and the one outlined by dotted line- to the tests with h_{max}= 200 nm. The residual trench left after FIB cross sectioning of the indentation at the lower left corner of the image is pointed to by an arrow.

20

Small outlined area at the lower right corner of the image encloses small sized indentations performed with h_{max}= 200 nm.
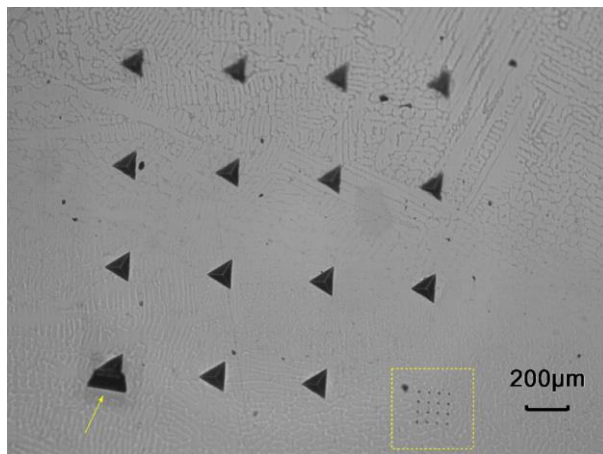

Figure 7. Optical image of the nanoindented and subsequently etched specimen EBM- manufactured from the SS316L+CF103 4/1 vol. powder blend. Core area of the sample. Larger indentation imprints are obtained with h_{max}= 2000 nm, smaller (bottom right, outlined area) with h_{max}= 200 nm. A residual trench of the FIB cross-sectioned indentation is pointed to by an arrow.

It is clear from the image in Figure 7 that the indentations performed at h_{max}= 2000 nm are large enough to involve several grains, including precipitated boundary phases. Therefore, the obtained response in terms of mechanical properties may be associated with the behavior of the overall structure of the material and can be correlated to the macroscopic properties. The corresponding hardness and stiffness values acquired for the two penetration depths on the EBM-manufactured: SS316L+CF103, SS316L+CF139 (both from 4/1 vol. ratios in the powder blend) and SS316L samples are presented in Table 4. Values are presented as an average from 16 nanoindentations and standard deviation.

Table 4. Average H and E values from 16 indentations measured at the core of EBM-manufactured SS316L and SS316L+Colferoloy 4/1 volume ratio samples with penetration depths of h_{max}=2000 nm (H_{2000},E_{2000}) and 200 nm (H_{200}, E_{200}) together with standard deviations.

	EBM SS316L + CF103	*EBM SS316L + CF139*	*EBM SS316L (Reference)*
$H_{200}(GPa)$	$6{,}9 \pm 0{,}7$	$7{,}0 \pm 0{,}4$	$5{,}7 \pm 0{,}9$
H_{2000} (GPa)	$4{,}0 \pm 0{,}1$	$4{,}0 \pm 0{,}1$	$2{,}9 \pm 0{,}2$
E_{200} (GPa)	$222{,}4 \pm 13{,}7$	$199{,}7 \pm 7{,}1$	$212{,}1 \pm 11{,}1$
E_{2000} (GPa)	$142{,}0 \pm 5{,}7$	$179{,}4 \pm 5{,}2$	$143{,}1 \pm 4{,}5$

Figure 8 presents the dependencies of the hardness (H) values on the penetration depth h calculated from the data of the nanoindentation tests with h_{max}= 2000 nm on the core of the EBM-manufactured SS316L and SS316L+Colferoloy 4/1 volume ratio samples. High hardness values are observed at small penetration depths, and the values gradually decrease as the indenter penetrates deeper into the material towards maximum depth.
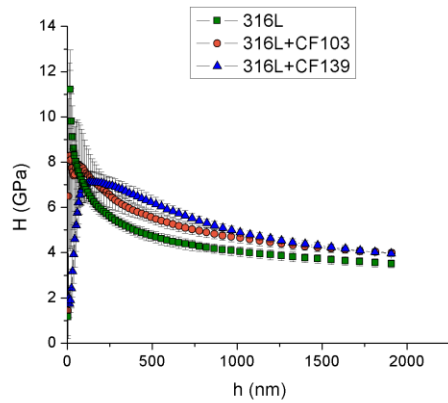

Figure 8. Dependence of the hardness H values on the nanoindenter penetration depth for indentations with h_{max}= 2000 nm. Core of the EBM- manufactured SS316L+Colferoloy CF103 sample.

As evident from Figure 8, such trend is especially pronounced for materials obtained from the powder blends as compared to SS316L reference material. Such behavior is commonly attributed to the so-called indentation size-effect [65], and is assumed to be a consequence of

dislocation nucleation phenomena at low penetration depths, and the interaction of dislocations with the grain boundaries in fine-grained materials.

A slight increase in the microhardness H, as measured at maximum indentation depth, is observed at SS316L+Colfereoly samples as compared to pure SS316L (Table 4). Furthermore, differences are especially pronounced for the first 1000 nm of penetration depth (Figure 8). It can be speculated that the precipitated boundary phases act as an effective barrier for the dislocation movement, which partly explain the observed increase in the hardness values. Another factor contributing to the observed hardening is the intrinsic harder and stronger nature of the boundaries determined by the precipitation of a Boron-enriched phase.

This becomes clear if the hardness values are associated with particular nanoindentations performed with h_{max}=200 nm (Figure 9).
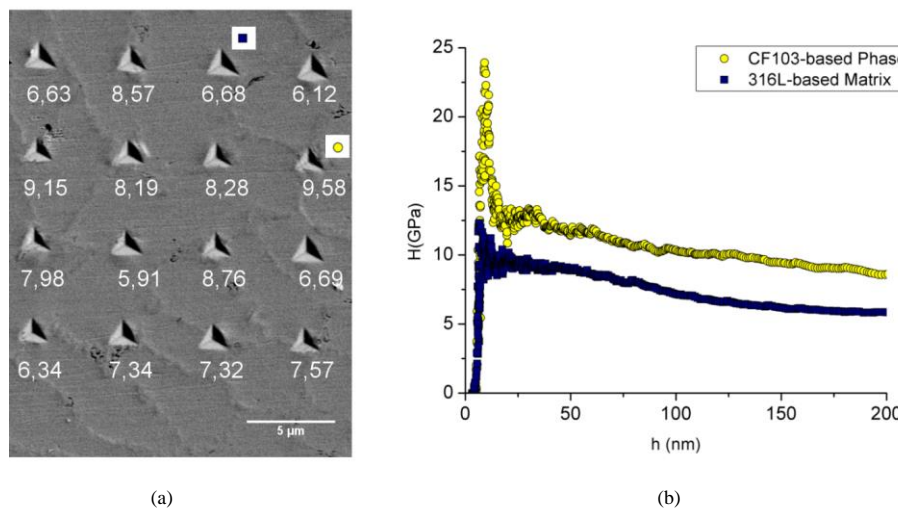

(a)   (b)

Figure 9. Matrix of nanoindentation traces performed with h_{max}=200 nm on the core of EBM-manufactured SS316L+Colferoloy CF103 sample. (a) Hardness values [GPa] are included next to corresponding indentation imprints. (b) Plots of the hardness dependence with penetration depth for individual indentations placed inside a grain (squares) and at the grain boundary phase (circles).

Difference in residual imprint sizes and measured hardness values between the individual indentations falling on the boundaries (CF-rich phase) and inside grains (austenitic SS316L-

23

dominated phase) are quite clear from the values given in Figure 9a. Two individual indents marked with a square (inside a grain) and circle (at a triple junction of the grain boundary phase) present a representative example.

Interestingly, we have recorded a decrease in measured ~~stiffness~~modulus of elasticity, E with the penetration depth larger than 100-200 nm. However, one can claim rather low reliability of the true E value recovery from the nanoindentation data, such behavior is generally not expected for isotropic dense materials. With the hardness measurement, plastic deformation fields are confined to a small volume under the indentation. However, in the case of the modulus of elasticity ~~stiffness~~ measurements, the elastic fields are significantly larger and the measured E value can be affected by factors both intrinsic and extrinsic to the material. In present case, observed drop in E value could be partially attributed to three factors: the encapsulation of the samples into the resin, which is significantly softer than tested material, presence of the residual porosity in the sample, and typical anisotropy of PBF AM materials, where the stiffness is commonly lower in build direction due to elongated columnar grain growth. It also deserves to be highlighted that at low penetration depths, where the effect of the factors mentioned above is minimal, SS316L+CF103 and SS316L+CF139 samples show stiffness values similar to the ones for the reference SS316L material.

Figure 10 presents a high resolution SEM image of the FIB cross-section performed at a selected nanoindentation imprint at h_{max}=2000 nm on the SS316L+CF103 sample (specific indentation is pointed to by an arrow in Figure 7).
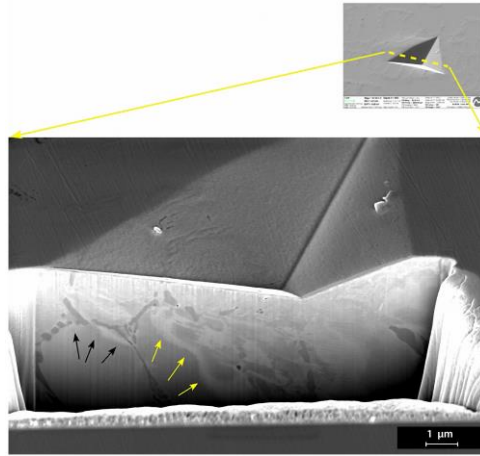
Figure 10. FIB cross-section of a nanoindentation imprint performed with h_{max}=2000 nm on SS316L+CF103 sample.

The very fine "polishing" achieved with the FIB technology is nicely revealing the material microstructure in the trench cross-section such as a rounded SS316L-based austenitic grains (light grey) and the precipitated grain boundary phase (dark grey). Furthermore, an extra microstructural feature (white-colored, pointed by arrows in Figure 10) appearing inside the grains in a region adjacent to the residual nanoindentation imprint is also revealed. Such features are becoming larger in width when moving from a region under one of the corners of the indentation towards its center, where maximum penetration is achieved. One can speculate that it is a dislocation network produced by the nanoindentations contrasted by the interaction of the Ga+ ions with the material during FIB fine polishing. If this explanation is accepted, one can further speculate that under the corner of the indentation the dislocation front is contained within the grain boundary (pointed by light arrows), and it further propagates inside the material towards maximum penetration depth area (pointed by dark arrows). This observation is in agreement with the known interaction of dislocations with grain boundary-precipitated

25

phase and its effect on materials hardening observed in this work and reported previously both

for L-PBF and EBM manufactured SS316L materials.

4.5 Corrosion Tests

Significant interest is caused to comparing corrosion properties of the materials manufactured using AM and traditional methods. Tests on SS316L additively manufactured with laser- based additive methods have confirmed its high corrosion stability, but revealed the anisotropy of corrosion properties linked to the corresponding anisotropy of material microstructure [67–71]. We have performed preliminary corrosion tests of the as manufactured by EBM SS316L+C103 and SS316L+C139 samples and compared the results to the ones of EBM manufactured SS316L samples.

Tables 5 and 6, and Figures 11 and 12 present the results of such comparison.

Table 5: Summary of the electrochemical corrosion measurements data

	E_r [mV] after 1 hr. vs SCE	i_t [mA/cm^2]	E_b [mV] vs SCE	E_V [mV] vs SCE	E_b-E_r [mV]	E_p [mV] vs SCE
SS316L	+80		500	650	420	-
SS316L+C103	+75	~1	250	500	175	-
SS316L+C139	-250		-40	50	210	-

Table 6. Corrosion test conditions

parameter	value
Test Cell	standard cell for electrochemical measurements (Fig. 9) with 1 liter of test solution
Test Solution	3% NaCl (DI water)
Deaerating	NO
Test Temperature	Room Temp.
E_r equilibrium	1 mV/min variation
Potentiostat	VersaSTAT 3 PotentiostatGalvanostat
Auxiliary Electrodes	Graphite (X2)
Reference Electrode	Saturated Calomel Electrode (sat'dKCl) - SCE

E_r – Rest Potential (open circuit condition – 1hrs.)
I_t – Threshold Current Density.
E_b - Breakdown Potential.
E_v – Vertex Potential
E_p – Protection potential at which the reverse scan intersects the forward scan.
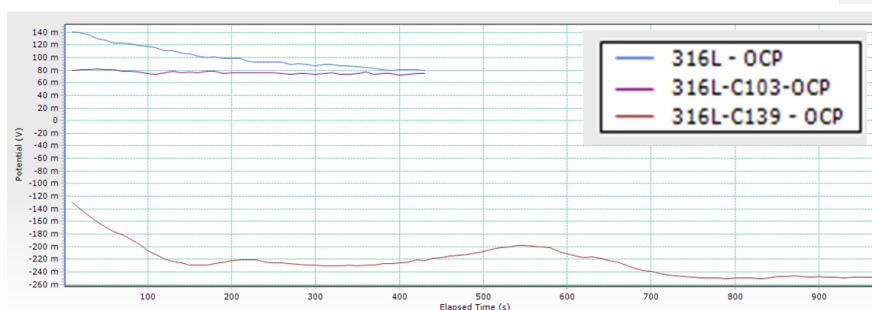
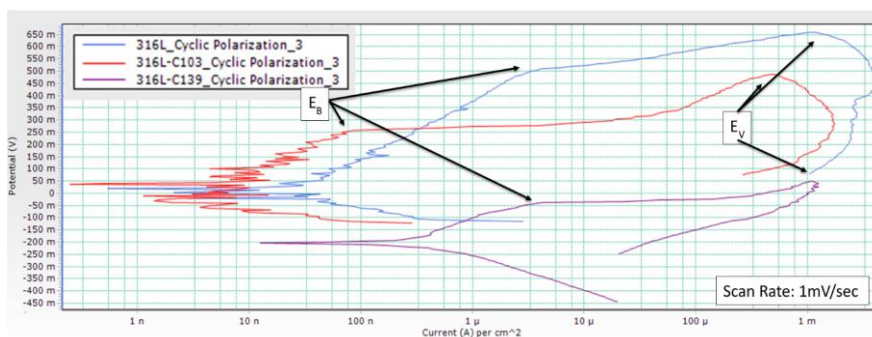Figure 11. Open Circuit Potential (Corrosion Potential) Curves

Figure 12. Cyclic Polarization Curves of the tested samples

Open Circuit Potential is a thermodynamic factor, which correlates with tendency to general corrosion. For SS316L-C139 sample, open-circuit potential is much lower than that of other samples, so from the perspective of thermodynamics samples made from the powder blends of SS316L and Colferoloys should have stronger tendency to general corrosion. Breakdown Potential (E_B) is the parameter correlating with the resistance to localized corrosion. For stainless steels like SS316L localized attack (pitting, crevice, etc.) is a dominant mechanism for corrosion. Parts with addition of Colferoloy have higher corrosion susceptibility than pure SS316L, with lowest local corrosion resistance for SS316L+C139. Polarization curve for SS316L+C139 is located in the graph to the right of other curves (higher current densities by approximately one decade) indicating that for this sample corrosion rate (general corrosion) will be higher. For all samples, the reverse scan path in the plots does not intersect with forward scans indicating that there is no re-passivation of the surfaces after the breakdown.

Summarizing the preliminary results of corrosion tests one can conclude that there is a slight corrosion resistance degradation of the sample SS316L+C103 (containing 0.60% Carbon) in comparison to pure SS316L one Manufactured by EBM. Corrosion resistance of the SS316L+C139 sample (containing 0.75% Carbon) is becoming significantly lower than that of SS316L. It can also be concluded that more thorough corrosion and abrasion resistance tests

5. Conclusions

Using powder blends for *in situ* alloying with powder bed fusion AM manufacturing was initially proposed as an approach with the potential of reducing the dependence upon the availability of corresponding pre-alloyed powders. Experiments with EBM of powder blends of SS316L and Colferoloys 103 and 139 with volumetric blending ratios of 4/1 and 4/3 were carried out in ARCAM EBM A2 machine using special setup optimized for the small powder batches. Thorough microstructure analysis of the manufactured sample was carried out using scanning and transmission electron microscopy, electron dispersive spectroscopy, high-angle annular dark-field scanning transmission electron microscopy. Measurements of microhardness and elastic modulus were carried out using nanoindentation. Preliminary corrosion tests on the samples were also undertaken. It is shown that effective material microstructure tailoring by electron beam energy deposition rate control at different dimensional scales can be successfully achieved with the blended precursor powders, resulting in the components with composite-like and homogeneous sections. It is concluded that implementation of blended powder pathway in powder bed AM together with beam energy steering allows for an effective sample composition and microstructure control at different dimensional scale. Therefore, the implementation of 'blended powder pathway' in powder bed AM provides a possibility of manufacturing in single industrial process components with unique properties having the composite-like and homogeneous zones and effectively adding a "4th dimension" to "3D printing".

Continuing research will be aiming at further development of the methodology and optimizing of the process parameters. Additional research will be performed into thorough investigations of the factors influencing the corrosion and abrasion resistance of the composite-like and

homogeneous zones in the samples additively manufactured from the powder blends using beam energy deposition rate control.

Acknowledgments

Conflict of Interest

The authors declare that they have no conflict of interest.

References

[1]   Bourell, D., Kruth, J.P., Leu, M., Levy, G., Rosen, D., Beese, A.M., Clare, A., 2017. Materials for additive manufacturing. CIRP Annals. 66, 659-681. https://doi.org/10.1016/j.cirp.2017.05.009.

[2]   Huang, Z., Qi, W., Zhou, Y., Xu, C., Zhang, Z., Liu, J., Hu, G., 2017. Effect of Print Method Based on SLM Technology on the Microstructure and Property of 316L Stainless Steel. In: Han Y. (Eds.) Advances in Materials Processing. CMC 2017. Lecture Notes in Mechanical Engineering. Springer, Singapore, pp 157-164. https://doi.org/10.1007/978-981-13-0107-0_15

[3]   Murr, L.E., 2015. Metallurgy of additive manufacturing: Examples from electron beam melting. Additive Manufacturing. 5, 40-53. https://doi.org/10.1016/j.addma.2014.12.002

[4]   Koptyug, A., Rännar, L.-E., Bäckström, M., Surmenev, R., 2016. Additive manufacturing in metal: technology advances generate new research challenges. Nanotechnologies: development and applications, XXI century. 8, 12-25.

[5]   Koptyug, A., Bäckström, M., Botero, C., Popov, V., Chudinova, E., 2018. Developing New Materials for Electron Beam Melting: Experiences and Challenges, Materials Science Forum. 941, 2190-2195. https://doi.org/10.4028/www.scientific.net/MSF.941.2190

[6]   Katz-Demyanetz, A., Popov ,V.V., Kovalevsky, A., Safranchik, D., Koptyug, A., 2019. Powder-bed Additive Manufacturing for aerospace application: techniques, metallic and metal/ceramic composite materials and trends. Manufacturing Rev. 5, #5. https://doi.org/10.1051/mfreview/2019003

[7]   Popov, V.V., Muller-Kamskii, G., Kovalevsky, A. Dzhenzhera, G., Strokin, E., Kolomiets, A., Ramon, J., 2018. Design and 3D-printing of titanium bone implants: brief review of approach and clinical cases. Biomed. Eng. Lett. 8, pp. 337-344. https://doi.org/10.1007/s13534-018-0080-5

[8]   Popov, V., Muller-Kamskii, G., Katz-Demyanetz, A., Kovalevsky, A., Usov, S., Trofimcow, D., Dzhenzhera, G., Koptyug, A., 2019. Additive manufacturing to veterinary practice: recovery of bony defects after the osteosarcoma resection in canines. Biomed. Eng. Lett. 9, pp. 97-108. https://doi.org/10.1007/s13534-018-00092-7.

[9]   Jaćimović, J., Binda, F., Herrmann, L.G., Greuter, F., Genta, J., Calvo, M., Tomše, T., Simon, R.A., 2017. Net Shape 3D Printed NdFeB Permanent Magnet. Adv. Eng. Mater. 19, 1700098. https://doi.org/10.1002/adem.201700098

[10]   Popov, V., Koptyug, A., Radulov, I., Maccari, F., Muller, G., 2018. Prospects of additive manufacturing of rare-earth and non-rare-earth permanent magnets. Procedia Manufacturing. 21, pp. 100-108. https://doi.org/10.1016/j.promfg.2018.02.199.

[11]   Radulov, I., Popov, V., Koptyug, A., Maccari, F., Gassmann, J., Essel, S., Kovalevsky, A., Skokov, K., Gutfleisch, O., Bamberger, M., 2019. Production of net-shape Mn-Al permanent magnets by electron beam melting. Additive Manufacturing. (Accepted manuscript).

[12]   Yi, M., Xu, B.X., Gutfleisch, O., 2019. Computational study on microstructure evolution and magnetic property of laser additively manufactured magnetic materials. Comput. Mech. 1–19. https://doi.org/10.1007/s00466-019-01687-2

[13]   Popov, V., Katz-Demyanetz, A., Koptyug, A., Bamberger, M., 2019. Selective Electron Beam Melting of Al0.5CrMoNbTa0.5 High Entropy Alloys using elemental powder blend. Heliyon. 5, e01188. https://doi.org/10.1016/j.heliyon.2019.e01188

[14]   Koptyug, A., Rännar, L.-E., Botero, C., Bäckström, M., Popov, V., 2018. Unique Material Composition Obtained By Electron Beam Melting Of Blended Powders. Proc. of Euro

PM2018 Congress &Exhibition,. Bilbao, Spain, October 2018. ISBN: 978-1-899072-50-7 (electronic).

[15]   Dehoff, R.R., Kirka, M.M., Sames, W.J., Bilheux, H., Tremsin, A.S., Lowel, L.E., Babu, S.S., 2015. Site specific control of crystallographic grain orientation through electron beam additive manufacturing. Materials Science and Technology. 31, pp. 931-938. https://doi.org/10.1179/1743284714Y.0000000734

[16]   Roehling, T.T., Wu, Sh.S.Q., Khairallah, S.A., Roehling, J.D., Soezeri, S.S., Crumb, M.F., Matthews, M.J., 2017. Modulating laser intensity profile ellipticity for microstructural control during metal additive manufacturing. Acta Materialia 128 (2017) 197e206. https://doi.org/10.1016/j.actamat.2017.02.025

[17]   Xu, W., Lui, E.W., Pateras, A., Qian, M., Brandt, M., 2017. In situ tailoring microstructure in additively manufactured Ti-6Al-4V for superior mechanical performance. Acta Materialia. 125, pp. 390–400. https://doi.org/10.1016/j.actamat.2016.12.027

[18]   Yan, F., Xiong, W., Faierson, E.J., 2017. Grain Structure Control of Additively Manufactured Metallic Materials. Materials. 10, 1260. https://doi.org/10.3390/ma10111260

[19]   Narra, S.P., Cunningham, R., Beuth, J., Rollett, A.D., 2018. Location specific solidification microstructure control in electron beam melting of Ti-6Al-4. Additive Manufacturing. 19, pp. 160–166. https://doi.org/10.1016/j.addma.2017.10.003

[20]   Saeidi, K., Gao, X., Zhong, Y., Shen, Z.J., 2015. Hardened austenite steel with columnar sub-grain structure formed by laser melting. Materials Science and Engineering A. 625, pp. 221–229. http://dx.doi.org/10.1016/j.msea.2014.12.018

[21]   Saeidi, K., Akhtar, F., 2018. Subgrain-controlled grain growth in the laser-melted 316L promoting strength at high temperatures. Royal Society Open Science. 5, 172394. https://doi.org/10.1098/rsos.172394

[22]   Piili, H., Happonen, A., Väistö., T., Venkataramanan, V., Partanen, J., Salminen, A., 2015.CostEstimationof Laser Additive Manufacturing of Stainless Steel. Physics Procedia. 78, pp. 388-396. https://doi.org/10.1016/j.phpro.2015.11.053

[23]   Wang, Y.M, Voisin, T., McKeown, J.T., Ye, J., Calta, N.P., Li, Z., Zeng, Z., Zhang, Y., Chen, W., Roehling, T.T, Ott, R.T., Santala, M.K, Depond, P.J., Matthews, M.J., Hamza, A.V., Zhu T., 2018. Additively manufactured hierarchical stainless steels with high strength and ductility. Nature Materials. 17, pp. 63-73. https://doi.org/10.1038/nmat5021

[24]   Sun, Z., Tan, X., Tor, S.B., Chua, C.K., 2018. Simultaneously enhanced strength and ductility for 3D-printed stainless steel 316L by selective laser melting. NPG Asia Materials. 10, pp. 127–136. https://doi.org/10.1038/s41427-018-0018-5

[25]   Gu, D., 2015. New metallic materials development by laser additive manufacturing. Laser Surface Engineering. pp. 163-180. http://dx.doi.org/10.1016/B978-1-78242-074-3.00007-6

[26]   Guo, P., Zou, B., Huang, C.Z., Gao, H.B., 2017. Study on microstructure, mechanical properties and machinability of efficiently additive manufactured AISI 316L stainless steel by high-power direct laser deposition. J. Mater. Process. Technol. 240, pp. 12-22. https://doi.org/10.1016/j.jmatprotec.2016.09.005

[27]   Rännar, L.-E., Koptyug, A., Olsén, J., Saeidi, K., Shen, Z., 2017. Hierarchical structures of stainless steel 316L manufactured by Electron Beam Melting. Additive Manufacturing. 17, pp. 106–112. https://doi.org/10.1016/j.addma.2017.07.003

[28]   Pham, M.S., Dovgyy, B., Hooper P.A., 2017. Twinning induced plasticity in austenitic stainless steel 316L made by additive manufacturing. Materials Science and Engineering A. 704, pp. 102–111. https://doi.org/10.1016/j.msea.2017.07.082

[29]   Zhong, Y., Rannar, L.-E., Liu, L., Koptyug, A., Wikman, S., Olsen, J., Cui, D., Shen, Z., 2017. Additive manufacturing of 316L stainless steel by electron beam melting for nuclear

fusion applications. Journal of Nuclear Materials. 486, pp. 234-245. https://doi.org/10.1016/j.jnucmat.2016.12.042

[30]   Günther, J., Brenne, F., Droste, M., Wendler, M., Volkova, O., Biermann, H., Niendorf, T., 2018. Design of novel materials for additive manufacturing – Isotropic microstructure and high defect tolerance. Scientific Reports. 8, pp. 1-14. https://doi.org/10.1038/s41598-018-19376-0

[31]   Kurzynowski, T., Gruber, K., Stopyra, W., Kuźnicka, B., Chlebus, E., 2018. Correlation between process parameters, microstructure and properties of 316 L stainless steel processed by selective laser melting. Materials Science and Engineering A. 718, pp. 64-73. https://doi.org/10.1016/j.msea.2018.01.103

[32]   Olsén, J., Shen, Z., Liu, L., Koptyug, A., Rännar, L.-E., 2018. Micro- and macro-structural heterogeneities in 316L stainless steel prepared by electron-beam melting. Materials Characterization. 141, pp. 1–7. https://doi.org/10.1016/j.matchar.2018.04.026

[33]   Segura, I.A., Mireles, J., Bermudez, D., Terrazas, C., Murr, L., Kun, L, Injeti, Y., Misra, R.D.K., Wicker, R.B., 2018. Characterization and mechanical properties of cladded stainless steel 316L with nuclear applications fabricated using electron beam melting. Journal of Nuclear Materials. 507, pp. 164-176. https://doi.org/10.1016/j.jnucmat.2018.04.026

[34]   Todd, I., 2018. Printing steels. Nature Materials. 17, pp. 13-14. https://doi.org/10.1038/nmat5042

[35]   Zhang, Ch., Wang, W., Li, Y., Yang, Y.-G., Yue, W., Liu, L., 2018. 3D printing of Fe-based bulk metallic glasses and composites with large dimension and enhanced toughness by thermal spraying. Journal of Materials Chemistry A. 6, pp. 6800-6805. https://doi.org/10.1039/C8TA00405F

[36]   Wang, C., Tan, X.P., Du, Z., Chandra, S., Sun, Z., Lim, C.W.J., Tor, S.B., Lim, C.S., Wong, C.H., 2019. Additive manufacturing of NiTi shape memory alloys using pre-mixed powders. Journal of Materials Processing Technology. 271, pp. 152-161. https://doi.org/10.1016/j.jmatprotec.2019.03.025

[37]   Koptyug, A., Rännar, L.-E., Bäckström, M., Langlet, A., 2013. Bulk Metallic Glass Manufacturing Using Electron Beam Melting. In: Proceedings of the International Conference on Additive Manufacturing & 3D Printing, Nottingham, July 9-10, 2013. http://urn.kb.se/resolve?urn=urn:nbn:se:miun:diva-20588

[38]   Drescher, P., Seitz, H., 2015. Process ability of an amorphous metal alloy powder by electron beam melting. RTe Journal - Fachforum für Rapid Technologie. 2015. https://www.rtejournal.de/ausgabe12/4236

[39]   Mahbooba, Z., Thorsson, L., Unosson, M., Skoglund, P., West, H., Horn, T., Rock, C., Vogli, E., Harrysson, O., 2018. Additive manufacturing of an iron-based bulk metallic glass larger than the critical casting thickness. Applied Materials Today. 11, pp. 264-269. https://doi.org/10.1016/j.apmt.2018.02.011

[40]   Uhlmann, E., Bergmann, A., Gridin, W., 2015. Investigation on Additive Manufacturing of Tungsten Carbide-cobalt by Selective Laser Melting. Procedia CIRP. 35, pp. 8-15. https://doi.org/10.1016/j.procir.2015.08.060

[41]   Farayibi, P.K., Folkes, J., Clare, A., Oyelola, O., 2011. Cladding of pre-blended Ti–6Al–4V and WC powder for wear resistant applications. Surface and Coatings Technology. 206, pp. 372–377. https://doi.org/10.1016/j.surfcoat.2011.07.033

[42]   Peng, H., Liu, C., Guo, H., Yuan, Y., Gong, S., Xu, H., 2016. Fabrication of WCp/NiBSi metal matrix composite by electron beam melting. Materials Science and Engineering: A. 666, pp. 320-323. https://doi.org/10.1016/j.msea.2016.04.079

[43]   Tao, X., Yao, Z., Zhang, S., Liao, J., Liang, J., 2018. Investigation on microstructure, mechanical and tribological properties of in situ (TiB + TiC)/Ti composite during the electron

beam surface melting. Surface and Coatings Technology. 337, pp. 418-425. https://doi.org/10.1016/j.surfcoat.2018.01.054

[44]   Reichardt, A., Dillon, R.P., Borgonia, J.P.C., Shapiro, A.A., McEnerney, B.W., Momose, T., Hoseman, P., 2016. Development and characterization of Ti-6Al-4V to 304L stainless steel gradient components fabricated with laser deposition additive manufacturing. Materials and Design. 104, pp. 404-413. https://doi.org/10.1016/j.matdes.2016.05.016

[45]   Yan, L., Chen, X., Li, W., Newkirk, J., Liou, F., 2016. Direct laser deposition of Ti-6Al-4V from elemental powder blends. Rapid Prototyping Journal. 22, pp. 810-816. https://doi.org/10.1108/RPJ-10-2015-0140

[46]   Li, W., Chen, X., Yan, L., Zhang, J., Zhang, X., Liou, F., 2018. Additive manufacturing of a new Fe-Cr-Ni alloy with gradually changing compositions with elemental powder mixes and thermodynamic calculation. The International Journal of Advanced Manufacturing Technology. 95, pp. 1013-1023. https://doi.org/10.1007/s00170-017-1302-1

[47]   Vora, P., Mumtaz, K., Todd, I., Hopkinson, N., 2015. AlSi12 in situ alloy formation and residual stress reduction using anchorless selective laser melting. Additive Manufacturing. 7, pp. 12-19. https://doi.org/10.1016/j.addma.2015.06.003

[48]   Fischer, M., Joguet, D., Robin, G., Peltier, L., Laheurte, P., 2016. In situ elaboration of a binary Ti–26Nb alloy by selective laser melting of elemental titanium and niobium mixed powders. Materials Science and Engineering C. 62, pp. 852–859. https://doi.org/10.1016/j.msec.2016.02.033

[49]   Wenjun, G., Chao G., Feng L., 2015. Microstructures of Components Synthesized via Electron Beam Selective Melting Using Blended Pre-Alloyed Powders of Ti6Al4V and Ti45Al7Nb. Rare Metal Materials and Engineering. 44, pp. 2623-2627. https://doi.org/10.1016/S1875-5372(16)60006-1

[50]   Guo, C., Ge, W., Lin, F., 2015. Dual-Material Electron Beam Selective Melting: Hardware Development and Validation Studies. Engineering, 1, pp. 124 -130. https://doi.org/10.15302/J-ENG-2015013

[51]   Tan, C., Wang, C., Wang, S., Wang, G., Ji, L., Tong, Y., Duanad, X., 2017. Investigation on 316L/316L-50W/W plate functionally graded materials fabricated by spark plasma sintering. Fusion Engineering and Design. 125, 171-177. https://doi.org/10.1016/j.fusengdes.2017.08.001

[52]   Yan, W., Ge, W., Smith, J., Lin, S., Kafka, O., Lin, F., Liu, W., 2016. Multi-scale modeling of electron beam melting of functionally graded materials. Acta Materialia. 115, pp. 403-412. https://doi.org/10.1016/j.actamat.2016.06.022

[53]   Lima, M.J.S., Silva, F.E.S., Lima, H.D., Souto, M.V.M., Filgueira, M., Souza, C.P., Gomes, U.U., 2018. Spark Plasma Sintering-SPS of Nanostructured Composite Powders (Wc-Ni) and Characterization Microstructural. Proc. Euro PM-2018, Bilbao, Spain, 14-18 October 2018.

[54]   Fernández-Roiz, A., Zoz, A., Vargas, V.G., Martín, J.M., Queck, M., 2018. Development of a Process to Manufacture Spherical Nano reinforced Titanium Alloy Powders for Additive Manufacturing. Proc. Euro PM-2018, Bilbao, Spain, 14-18 October 2018.

[55]   Martin, J.H., Yahata, B.D., Hundley, J.M., Mayer, J.A., Schaedler, T.A., Pollock, T.M., 2017. 3D printing of high-strength aluminium alloys. Nature. 549, pp. 365–369. https://doi.org/10.1038/nature23894

[56]   Figiel, L.S., 1991. On Damascus Steel. Atlantis Arts Press, 1991. ISBN-13: 978-0962871115.

[57]   Arcam EBM, A GE additive company, Available from http://www.arcam.com/

[58]   Carpenter Technology Corporation, Available from https://www.cartech.com/en/locationaddress/carpenter-powder-products-ab/

[59]   Wall Colmonoy Company, Available from https://www.wallcolmonoy.com/

[60]   Uozato, S., Nakata, K., Ushio, M., 2005. Evaluation of ferrous powder thermal spray coatings on diesel engine cylinder bores. Surface & Coatings Technology. 200, pp. 2580 -2586. https://doi.org/10.1016/j.surfcoat.2005.05.042

[61]   Bolelli, G., Bonferroni, B., Laurila, J., Lusvarghi, L., Milanti, A., Niemi, K., Vuoristo, P., 2012. Micromechanical properties and sliding wear behavior of HVOF-sprayed Fe-Based alloy coatings. Wear. 276-277, pp. 29-47. https://doi.org/10.1016/j.wear.2011.12.001

[62]   Bolelli, G., Börner, T., Milanti, A. , Lusvarghi, L., Laurila, J., Koivuluoto, H., Niemi, K., Vuoristo, P., 2014. Tribological behavior of HVOF- and HVAF-sprayed composite coatings based on Fe-Alloy + WC–12% Co. Surface and Coatings Technology. 248, pp. 104-112. https://doi.org/10.1016/j.surfcoat.2014.03.037

[63]   Vock, S., Klöden, B., Kirchner, A., Weißgärber, T., Kieback, B., 2019. Powders for powder bed fusion: a review. pp. 1-15. https://doi.org/10.1007/s40964-019-00078-6

[64]   Tammas-Williams, S., Zhao, H., Léonard, F., Derguti, F., Todd, I., Prangnell, P.B., 2015. XCT analysis of the influence of melt strategies on defect population in Ti–6Al–4V components manufactured by Selective Electron Beam Melting. Materials Characterization. 102, pp. 47–61. https://doi.org/10.1016/j.matchar.2015.02.008

[65]   Oliver, W.C., Pharr, G.M., 2004. Measurement of hardness and elastic modulus by instrumented indentation: Advances in understanding and refinements to methodology. J. Mater. Res. 19, pp. 3–20. https://doi.org/10.1557/jmr.2004.19.1.3

[66]   Pharr, G.M., Herbert, E.G., Gao, Y., 2010. The Indentation Size Effect: A Critical Examination of Experimental Observations and Mechanistic Interpretations. Annu. Rev. Mater. Res. 40, pp. 271–292. https://doi.org/10.1146/annurev-matsci-070909-104456

[67]   Sander, G., Thomas, S., Cruz, V., Jurg, M., Birbilis, N., Gao, X., Brameld, M., Hutchinson, C.R., 2017. On the corrosion and metastable pitting characteristics of 316L stainless steel produced by selective laser melting. J. Electrochem. Soc. 164, C250-C257. https://doi.org/10.1149/2.0551706jes

[68]   Trelewicz, J.R., Halada, G.P., Donaldson, O.K., Manogharan, G., 2016. Microstructure and corrosion resistance of laser additively manufactured 316L stainless steel. JOM. 68, pp. 850-859. https://doi.org/10.1007/s11837-016-1822-4

[69]   Ni, X.Q., Kong, D.C., Wu, W.H., Zhang, L., Dong, C.F., He, B.B., Lu, L., Wu, K.Q., Zhu, D.X., 2018. Corrosion behavior of 316L stainless steel fabricated by selective laser melting under different scanning speeds. J. Mater. Eng. Perform. 27, pp. 3667-3677. https://doi.org/10.1007/s11665-018-3446-z

[70]   Ni, X.Q., Kong, D.C., Wen, Y., Zhang, L., Wu, W.H., He, B., Lu, L., Zhu, D., 2019. Anisotropy in mechanical properties and corrosion resistance of 316L stainless steel fabricated by selective laser melting. International Journal of Minerals, Metallurgy, and Materials. 26, pp. 319- 328. https://doi.org/10.1007/s12613-019-1740-x

[71]   Man, C., Duan, Z., Cui, Z., Dong, C., Kong, D., Liu, T., Chen, S., Wang, X., 2019. The effect of sub-grain structure on intergranular corrosion of 316L stainless steel fabricated via selective   laser   melting.   Materials   Letters.   243,   pp.   157-160. https://doi.org/10.1016/j.matlet.2019.02.047